FRONTIERS OF PHYSICS

RESEARCH ARTICLE
Volume 19 / Issue 3 / 32205 / 2024

High-resolution recognition of FOAM modes via an improved EfficientNet V2 based convolutional neural network

Youzhi Shi[1], Zuhai Ma[1], Hongyu Chen[1], Yougang Ke[3], Yu Chen[1,†], Xinxing Zhou[2,‡]

1 International Collaborative Laboratory of 2D Materials for Optoelectronics Science and Technology,
Institute of Microscale Optoelectronics, Shenzhen University, Shenzhen 518060, China
2 Key Laboratory of Low-Dimensional Quantum Structures and Quantum Control of Ministry of Education,
Synergetic Innovation Center for Quantum Effects and Applications, School of Physics and Electronics,
Hunan Normal University, Changsha 410081, China
3 Key Laboratory of Hunan Province on Information Photonics and Freespace Optical Communications,
School of Information Science and Engineering, Hunan Institute of Science and Technology,
Yueyang 414006, China
Corresponding authors. E-mail: †yuchen@szu.edu.cn, ‡xinxingzhou@hunnu.edu.cn

Received September 26, 2023; accepted November 24, 2023

© Higher Education Press 2024

ABSTRACT

Vortex beam with fractional orbital angular momentum (FOAM) is the excellent candidate for improving the capacity of free-space optical (FSO) communication system due to its infinite modes. Therefore, the recognition of FOAM modes with higher resolution is always of great concern. In this work, through an improved EfficientNetV2 based convolutional neural network (CNN), we experimentally achieve the implementation of the recognition of FOAM modes with a resolution as high as 0.001. To the best of our knowledge, it is the first time this high resolution has been achieved. Under the strong atmospheric turbulence (AT) ($C_n^2 = 10^{-15}$ m$^{-2/3}$), the recognition accuracy of FOAM modes at 0.1 and 0.01 resolution with our model is up to 99.12% and 92.24% for a long transmission distance of 2000 m. Even for the resolution at 0.001, the recognition accuracy can still remain at 78.77%. This work provides an effective method for the recognition of FOAM modes, which may largely improve the channel capacity of the free-space optical communication.

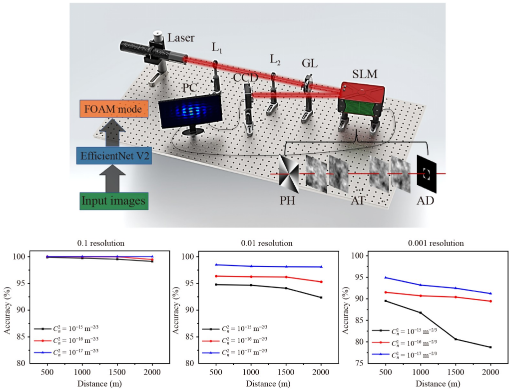

Keywords OAM, free-space optical communication, deep learning, convolutional neural network

1 Introduction

The vortex beams (VBs) can be characterized by a phase factor $\exp(il\varphi)$ and the orbital angular momentum (OAM) $l\hbar$ carried for each photon [1]. The VBs exhibit a spiral wave front and phase singularity at the center, where the $l, \hbar, \varphi$ represent the topological charge, the Planck constant and the azimuthal angle respectively. Due to these special characteristics and more manipulation dimension, the VBs have highly potential applications in quantum entanglement [2], sensing [3], super-resolution microscopy [4], biomedicine [5], nonlinear optics [6], and optical communication [7]. In a free-space optical communication (FSO) system [8–10], the transmission capability can be greatly expanded with the introduction of OAM, especially the fractional orbital angular momentum (FOAM) due to the theoretically infinite number of available OAM modes [11]. However, the

Higher Education Press

https://doi.org/10.1007/s11467-023-1373-4

slight difference in the radius of the central circular ring between adjacent modes poses a great challenge to the recognition of FOAM modes compared to the integer modes [12, 13]. Furthermore, in an OAM-FSO system, the atmospheric turbulence (AT) is a common harmful factor that causes the optical intensity fluctuation, random phase perturbation, and position displacement on the VB signal [14, 15]. Therefore, the high-resolution recognition of FOAM modes under strong AT is still a problem demanding prompt solution. Various methods have been proposed to recognize integer OAM modes [16–21] and FOAM modes at 0.1 resolution [22, 23]. However, achieving higher-resolution recognition of FOAM modes remains a challenging endeavor.

In recent years, deep learning (DL) has been widely used in computer vision [24–27]. Compared to other neural networks, convolutional neural network (CNN) [28, 29] possesses superior capabilities in feature extraction and image data processing, which are the critical factors in image recognition. By building a CNN with an 8-layer structure, the recognition of FOAM modes at 0.01 resolution was firstly achieved with the recognition accuracy more than 99% [30]. However, this architecture is not suitable under strong AT because it lacks a module for extracting detailed features from images. Then, a 50-layer network structure based residual neural network (ResNet 50, a common CNN architecture) was introduced to recognize the FOAM modes at 0.1 resolution under strong AT ($C_n^2 = 5\times10^{-14}\,\mathrm{m}^{-2/3}$) and long transmission distance (z = 1500 m). The recognition accuracy was as high as 85.30% [31]. By passing the FOAM through a column lens and then feeding it into the ResNet 50, the recognition resolution of FOAM modes was further improved to 0.01 even under strong AT ($C_n^2 = 10^{-15}\,\mathrm{m}^{-2/3}$) and long transmission distance (z = 1500 m). The recognition accuracy reached 99.07% at 0.1 resolution and 73.68% at 0.01 resolution [32]. However, the ResNet 50 will suffer overfitting and gradient vanishing easily when training large-scale datasets, which is unfriendly to the image recognition task with a high similarity [33]. Recently, the EfficientNet V2 based CNN has been demonstrated that it can achieve higher recognition accuracy in image classification by employing incremental learning methods and architectural improvements such as the squeeze-and-excitation (SE) module and self-attention mechanism [34–36]. Therefore, the EfficientNet V2 may help further improve the recognition accuracy of FOAM modes at higher resolution (like 0.001) even under strong AT and long transmission distance.

In this work, we experimentally achieve the recognition of FOAM modes at 0.1, 0.01, and 0.001 resolution with much high recognition accuracy under strong AT and long transmission distance by an improved EfficientNet V2 based CNN. By modifying the layers of the SE module and optimizing other parameters (dropout, width factor, depth factor, activation function, etc.), the improved model can extract more detail features of FOAM modes. Based on this proposed model, we experimentally verify its great effectiveness for the recognition of FOAM modes at 0.1 and 0.01 resolution with much high recognition accuracy. Most importantly, for the FOAM modes at 0.001 resolution, the recognition accuracy can still reach 78.77% even under strong AT ($C_n^2 = 10^{-15}\,\mathrm{m}^{-2/3}$) and long transmission distance (z = 2000 m). Our work exhibits the huge potential of CNN in the recognition of FOAM modes, which may promote the booming development of FSO communication.

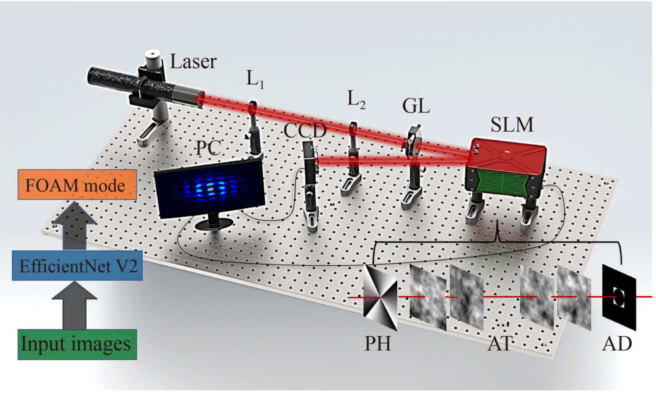

Fig. 1 Diagram of the experimental setup. L_1, L_2: Lens; GL: Glan prism polarizer; SLM: Spatial light modulator; CCD: Charge-coupled device; PH: Phase hologram of FOAM; AT: Atmospheric turbulence; AD: Aperture diaphragm.

2 Principles and concepts

2.1 Experimental setup

Figure 1 shows the experimental setup for generating and recognizing the FOAM modes. A highly stable He-Ne laser (wavelength: 632.8 nm; beam waist: 1.0 mm) is used as the Gaussian beam source. The beam is firstly expanded to 6 mm by the beam expansion system [formed by lens L_1 (50 mm) and L_2 (300 mm)]. A Glan–Teller (GL) prism is used to control the beam polarization. Then, the beam incidents on a spatial light modulator (SLM: Holoeye, ERIS-VIS-109), which is preloaded with the phase hologram of FOAM, AT, and AD. Finally, the diffraction pattern captured by the charge-coupled device (CCD: Thorlabs, BC106N-VIS/M) is input to the improved EfficientNet V2 model for recognizing the FOAM modes.

2.2 Intensity distribution of VBs after passing AD

FOAM modes (with topological charge l) can be easily obtained by loading the spiral wavefront phase on a Gaussian beam using SLM [37]

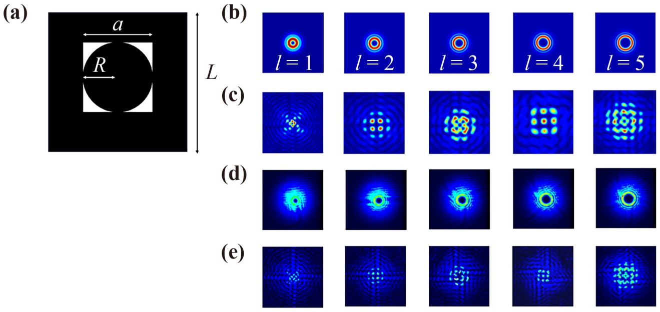

Fig. 2 **(a)** The structure of the AD. **(b)** Intensity distribution of original OAM modes ($l = 1$–5) by simulation. **(c)** Intensity distribution of OAM modes ($l = 1$–5) diffracting after the AD by simulation. **(d)** Intensity distribution of original OAM modes ($l = 1$–5) by experiment. **(e)** Intensity distribution of OAM modes ($l = 1$–5) diffracting after the AD by experiment.

$$E\left(r_0, \theta_0\right) = A \exp\left(-\frac{r_0^2}{w_0^2}\right) \exp\left(\mathrm{i} l \theta_0\right), \tag{1}$$

where (r_0, θ_0) denotes the cylindrical coordinate, A is the complex amplitude, w_0 is the waist of the Gaussian beam, and l is the topological charge.

In order to obtain more detailed features of the FOAM, we design an aperture diaphragm (AD) consisting of a square hole with an internal circular screen shown in Fig. 2(a). The transmittance function of AD can be expressed as

$$T\left(r_1, \theta_1\right) = f_1\left(r_1, \theta_1\right) + f_2\left(r_1, \theta_1\right), \tag{2}$$

$$f_1\left(r_1, \theta_1\right) = \begin{cases} 1, & r < a \times \sec\left(\dfrac{\pi}{4}\right) \\ 0, & \text{others}, \end{cases}, \tag{3}$$

$$f_2\left(r_1, \theta_1\right) = \begin{cases} 1, & r < R, \\ 0, & \text{others}, \end{cases} \tag{4}$$

where f_1 and f_2 are the transmittance functions of the square hole and circular screen, respectively, a is the side length of the square hole, and R is the radius of circular screen. In this work, $R = a/2 = 1.5$ mm.

According to the Collins diffraction integral equation [38, 39], the field distribution of the VB after passing through the AD can be expressed as

$$\begin{aligned} U\left(r, \theta, z\right) = {} & \frac{\exp\left(\mathrm{i}kz\right)}{\mathrm{i}\lambda z} \int_0^{\infty} \int_0^{2\pi} E(r_0, \theta_0) T\left(r_1, \theta_1\right) \\ & \times \exp\left(\frac{\mathrm{i}k}{2z}\left[r_0^2 + r_1^2 - 2 r_0 r_1 \cos\left(\theta_0 - \theta_1\right)\right]\right) r_0 \mathrm{d}r_0 \mathrm{d}\theta_0, \end{aligned} \tag{5}$$

where z is the transmission distance.

Finally, the beam intensity received on the CCD can be expressed as

$$I(r, \theta, z) = U(r, \theta, z) \times U^*(r, \theta, z). \tag{6}$$

To verify the effectiveness of our designed AD, we give out the simulation and experimental results of OAM modes in Fig. 2. Figures 2(b) and (c) show the simulated intensity distributions of the original OAM modes ($l = 1$–5) and diffraction patterns after AD. In Fig. 2(b), the radius of center ring increases gradually with the increase of l. After the AD, the diffraction patterns in Fig. 2(c) present a four-fold symmetry [40], arising from the square diaphragm contained in AD. When $l > 1$, the number of diffracted spots in the outermost layer is $(l + 1)/2$ (when l is odd), or $(l + 2)/2$ (when l is even). In addition, whether there are intersection points in the center region can also determine the even or odd value of l (When l is odd, the intersection point appears). For example, when $l = 3$, the number of diffracted spots in the outermost layer is 2, and there are four intersection points in the center.

2.3 Construction of AT

During the beam transmission, the AT can seriously distort the wavefront phase and intensity distribution of the VB, which brings serious disturbance to the OAM communication [41, 42]. Here, we use the Hill Andrews model to simulate the AT, the equivalent phase can be shown as [43]

$$\begin{aligned} \Phi_n\left(k\right) = {} & 0.33 C_n^2 \left[1 + 1.802 \sqrt{\frac{k^2}{k_l^2}} - 0.254 \left(\frac{k^2}{k_l^2}\right)^{\frac{7}{12}}\right] \\ & \times \frac{\exp\left(-\dfrac{k^2}{k_l^2}\right)}{\left(k_0^2 + k^2\right)^{\frac{11}{6}}}, \end{aligned} \tag{7}$$

where $k_0 = 2\pi/L_0$, L_0 is the outer scale of AT, $k_l = 2\pi/l_0$, l_0 is the inner scale of AT, $k^2 = k_x^2 + k_y^2$, k_x and k_y denote the wavenumbers in the x and y directions, respectively, and C_n^2 is the structure constant of the refractive index of air which describes the intensity of AT [44].

The spatial variation in AT ($\sigma^2(k)$) can be approximated by a number of phase screens, which modify the phase profile as the beam transmission. The relationship between $\sigma^2(k)$ and $\Phi_n(k)$ can be expressed as [45]

$$\sigma^2(k) = \left(\frac{2\pi}{N\Delta x}\right)^2 2\pi k_z^2 \Delta z \Phi_n(k), \tag{8}$$

where Δx denotes the grid spacing of a random phase screen, N indicates the phase screen size, Δz is the interval distance between adjacent phase screens, and $k_z = 2\pi/\lambda$. We utilize a fast Fourier transform (FFT) operation to express the phase screen in the frequency domain,

$$\xi\left(k\right) = FFT\left(M\sigma(k)\right), \tag{9}$$

where M is a complex Gaussian random matrix with mean 0 and variance 1 in the frequency domain, and

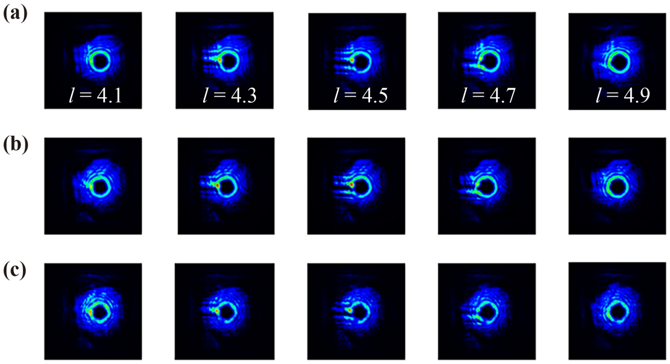

Fig. 3 Intensity of FOAM modes ($l = 4.1, 4.3, 4.5, 4.7, 4.9$) under three different intensities of AT and transmission distance ($z = 2000$ m). Rows **(a–c)** show the intensity of the FOAM modes under AT ($C_n^2 = 10^{-17}$ m$^{-2/3}$, $C_n^2 = 10^{-16}$ m$^{-2/3}$ and $C_n^2 = 10^{-15}$ m$^{-2/3}$), respectively.

FFT represents the fast Fourier transform operation.

During the beam transmission, the phase information of each layer can be designed and superimposed on the SLM. It should be noted that as the interval distance Δz between the adjacent phase screens decreases, the simulation accuracy increases rapidly. However, the computational resource requirement increases significantly, which is not conducive to the collection of large data sets. After several tests, we finally chose $\Delta z = 250$ m. The inner scale and outer scale of AT are set to $l_0 = 0.01$ m and $L_0 = 100$ m. Figure 3 shows the intensity of FOAM modes under three different AT and transmission distance ($z = 2000$ m) experimentally. As C_n^2 increases, the intensity of FOAM modes undergoes increasingly obvious distortions which enlarges the challenge of recognizing.

2.4 Architecture of the improved EfficientNet V2 based CNN

Noting that some components of the EfficientNet V2 model like SE module is useful for analyzing the detailed features of images. Therefore, for higher recognition resolution and accuracy, we increase the layers of the SE module and optimize other parameters (dropout, width factor, depth factor, activation function, etc.) to extract more detail feature of the FOAM modes.

The architecture of the CNN is shown in Fig. 4(a), where the input image size is adjusted to 224×224, Conv3×3 is the 3×3 convolution + activation function (SiLU) + Batch Normalization (BN). The Fused-MBConv module enhances the CNN performance by combining feature maps of different resolutions. When expansion is set to 1 [Fig. 4(b)], it consists of a 3×3 convolutional layer, a BN layer with SiLU activation, and a dropout layer with 0.2 dropout rate. In the case of expansion $\neq 1$ [Fig. 4(c)], it includes an additional Project Conv module. By using these two different expansion ratios (1 and $\neq 1$), the CNN can achieve faster training and manage complexity efficiently in image recognition. The structure of the MBConv module is shown in Fig. 4(d), compared to Fused-MBConv module, it has an additional SE module, which means it can automatically learn the importance of different channel features. 0.25 represents that the node number of the first fully connected layer in the SE module occupies 25% of the input MBConv module feature matrix channels. The key distinction between the MBConv and Fused-MBConv modules lies in the incorporation of fused point-wise and depth-wise convolution, which enhances the computational efficiency and network performance in the

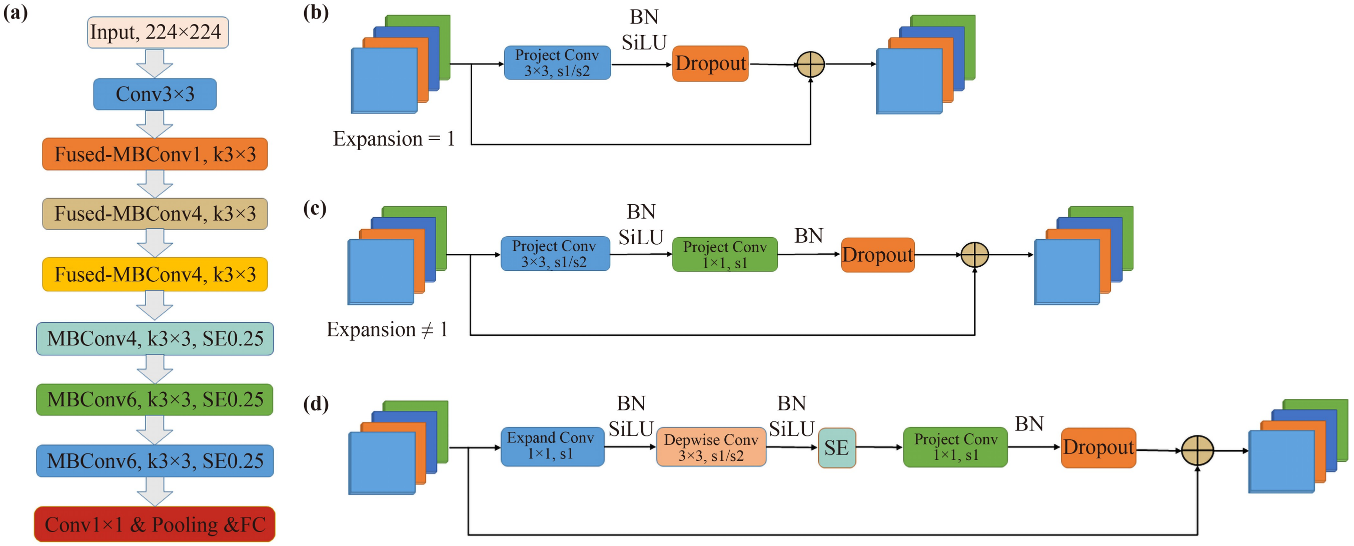

Fig. 4 Schematic diagram of the structure of the EfficientNet V2 model. **(a)** Flowchart of the EfficientNet V2 model. **(b)** Structure diagram of the Fused-MBConv module (Expansion = 1). **(c)** Structure diagram of the Fused-MBConv module (Expansion $\neq 1$). **(d)** Structure diagram of the MBConv module.

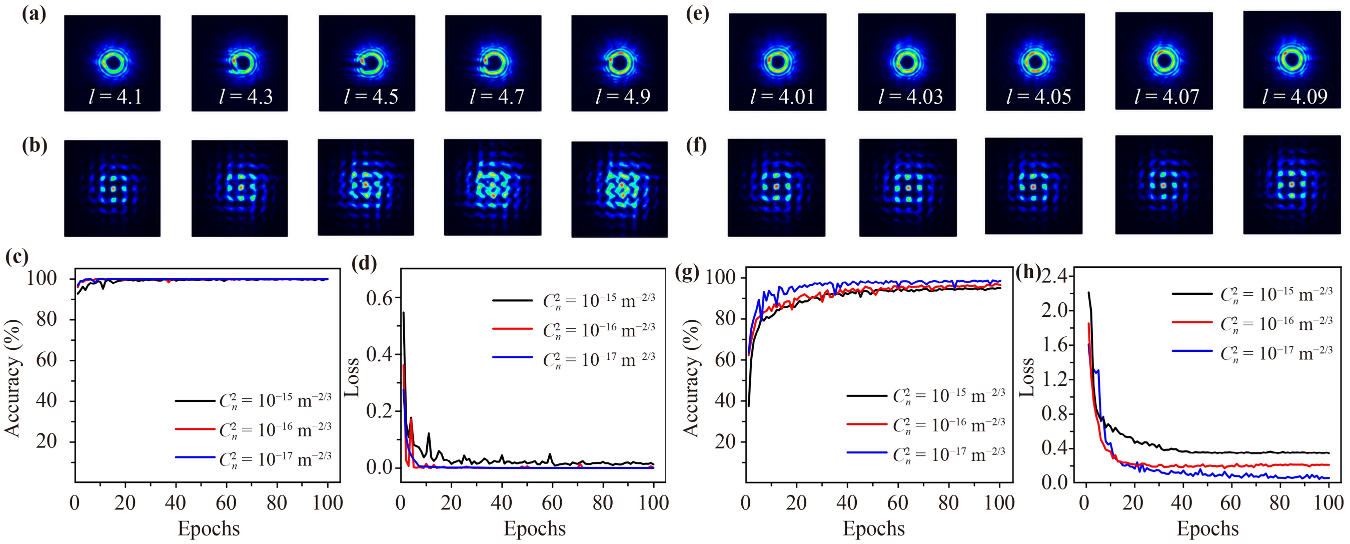

Fig. 5 Test results of 0.1 and 0.01 resolution FOAM modes at $z = 500$ m. **(a, e)** Original FOAM modes of 0.1 and 0.01 resolution at $C_n^2 = 10^{-16}$ m$^{-2/3}$. **(b, f)** Diffraction patterns detected by CCD of 0.1 and 0.01 resolution. **(c, g)** Accuracy curves of 0.1 and 0.01 resolution FOAM modes in test set under different AT. **(d, h)** Loss curves of 0.1 and 0.01 resolution FOAM modes in test set under different AT.

latter.

In the end of the CNN model, a module consisting of a 1 × 1 convolutional layer + pooling layer + FC (fully connected layer, activation = Softmax) is used as the output for the classification of the FOAM modes. As for the loss function, we use the Sparse Categorical Cross Entropy [46], which can be expressed as

$$loss\left(f\left(X,b\right),Y\right) = -\frac{1}{m}\sum_{i=1}^{m} y_i \log(y^*), \tag{10}$$

where m is the number of data set input to the CNN, y^* is the predicted output, and y_i is the ideal output. The weight and bias parameters are updated using the Adam optimizer with a learning rate of 0.005, aiming to minimize the loss function.

3 Results and discussion

3.1 Recognition of FOAM modes at 0.1 and 0.01 resolution

For the FOAM modes at 0.1 resolution, we experimentally collect 10000 images (80% serving as the training sets and 20% as the test sets). Figures 5(a)–(d) show the recognition results under a medium AT ($C_n^2 = 10^{-16}$ m$^{-2/3}$) and transmission distance ($z = 500$ m) of FOAM modes at 0.1 resolution. Figure 5(a) presents the intensity distribution of FOAM modes transmitting under AT with $l = 4.1$, 4.3, 4.5, 4.7, and 4.9, respectively. As l increases, the radius of central circular ring increases and the size of the notch increases first and then decreases. The corresponding intensity distributions diffracting after the ADs are shown in Fig. 5(b). As l increases, the diffraction center gradually becomes a rectangular hole, and the rest of the diffracted spots gradually transition into the dart-shaped structures. It is worth noting that at this point, the topological charge l can still be recognized narrowly. After applying our proposed CNN, the recognition accuracy and loss values of the FOAM modes in the test set are shown in Figs. 5(c) and (d) (red line). For comparison, we also show the situation under $C_n^2 = 10^{-15}$ m$^{-2/3}$ (blackline) and $C_n^2 = 10^{-17}$ m$^{-2/3}$ (bule line). As a result, the recognition accuracy in test set can quickly approach 100% after only 3 epochs. After 20 epochs, the accuracy and loss curves under three different AT all tend to be stable. When the epochs exceed 100, the recognition accuracy of FOAM modes finally reach 99.80%, 100%, and 100% under three different AT, while the losses are 1.25×10^{-2}, 2.44×10^{-7}, and 1.57×10^{-7}. It is shown that our proposed CNN model exhibits perfect performance for the recognition of FOAM modes at 0.1 resolution under strong AT and long transmission distance.

For the FOAM modes at 0.01 resolution, we experimentally collect 25000 images (80% serving as the training set and 20% as the test set), results show in Figs. 5(e)–(h). From Fig. 5(e), the radius of the center ring of adjacent FOAM modes increases at a much slower rate than the FOAM modes at 0.1 resolution and the appearance of notches is barely visible. Figure 5(f) shows the intensity distribution of FOAM modes diffracting after AD. Unfortunately, it is not possible to directly distinguish the FOAM modes at 0.01 resolution. Then, our proposed CNN model is applied for the recognition of FAOM modes. From Figs. 5(g) and (h), after 40 epochs, the

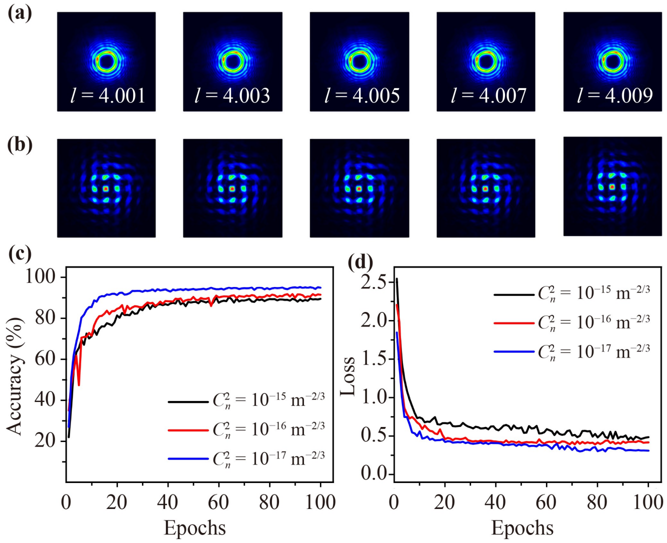

Fig. 6 Test results of 0.001 resolution FOAM modes at $z =$ 500 m. **(a)** Original FOAM modes and **(b)** diffraction patterns detected by CCD ($C_n^2 = 10^{-16}$ m$^{-2/3}$; $l = 4.001$, 4.003, 4.005, 4.007, 4.009). **(c)** Accuracy and **(d)** loss curves in test set under different AT.

recognition accuracy curve and loss curve in test set all become stably, the recognition accuracy of FOAM modes finally reaches 94.76%, 96.34%, and 98.46%, while the losses are 0.3411, 0.2038, and 0.0513 under three different AT. The model converges more slowly than that at 0.1 resolution. However, our model can still possess high performance at 0.01 resolution.

3.2 Recognition of FOAM modes at 0.001 resolution

Furtherly, the proposed CNN model is utilized in recognition of the FOAM modes at 0.001 resolution. Due to the more difficulty for the recognition of FAOM modes at higher resolution, we expand the number of data set to improve the recognition accuracy. We eventually collect 60 000 images, in which 48 000 are used as the training set and others as the test set. Figure 6 shows the recognition results under a medium AT of $C_n^2 = 10^{-16}$ m$^{-2/3}$ and transmission distance of $z = 500$ m at 0.001 resolution. Unfortunately, both from the radius of the center ring of the FOAM modes in Fig. 6(a) and from the spot distribution of the FOAM modes after AD in Fig. 6(b), the differences between adjacent FOAM modes are essentially invisible and can no longer be recognized. Nevertheless, our proposed CNN model can solve this problem. Figures 6(c) and (d) show the recognition accuracy and loss value in the test set under three different AT. Due to the increase in training difficulty, the recognition accuracy for the first few epochs dropped significantly comparing to the previous ones. However, since our proposed model has great advantages in performing feature extraction, it can still converge around 60 epochs. After 100 epochs, the recognition accuracy of FOAM modes under weak ($C_n^2 = 10^{-17}$ m$^{-2/3}$), medium ($C_n^2 = 10^{-16}$ m$^{-2/3}$), strong ($C_n^2 = 10^{-15}$ m$^{-2/3}$) AT are 94.88%, 91.48%, and 89.47%. The losses are 0.3102, 0.4271, and 0.4861. It can be concluded that our proposed model is still highly effective for the recognition of FOAM modes at 0.001 resolution, even under strong AT and long transmission distance.

Finally, we comprehensively investigate the effects of different transmission distance and AT on the recognition accuracy of FOAM modes. Figure 7(a) shows the recognition accuracy of FOAM modes at 0.1 resolution under different AT and transmission distances. As the AT increase, the recognition accuracy decreases slightly but still remains at a very high level. Even under strong AT ($C_n^2 = 10^{-15}$ m$^{-2/3}$) and long distance ($z = 2000$ m), the recognition accuracy is still up to 99.12%. From the above results, our model is extremely effective in recognizing FOAM modes at 0.1 resolution. Figure 7(b) shows the recognition accuracy of FOAM modes at 0.01 resolution. Obviously, even under strong AT ($C_n^2 = 10^{-15}$ m$^{-2/3}$) and long transmission distance ($z = 2000$ m), the recognition accuracy reaches 92.24%. As anticipated, the recognition accuracy of FOAM modes

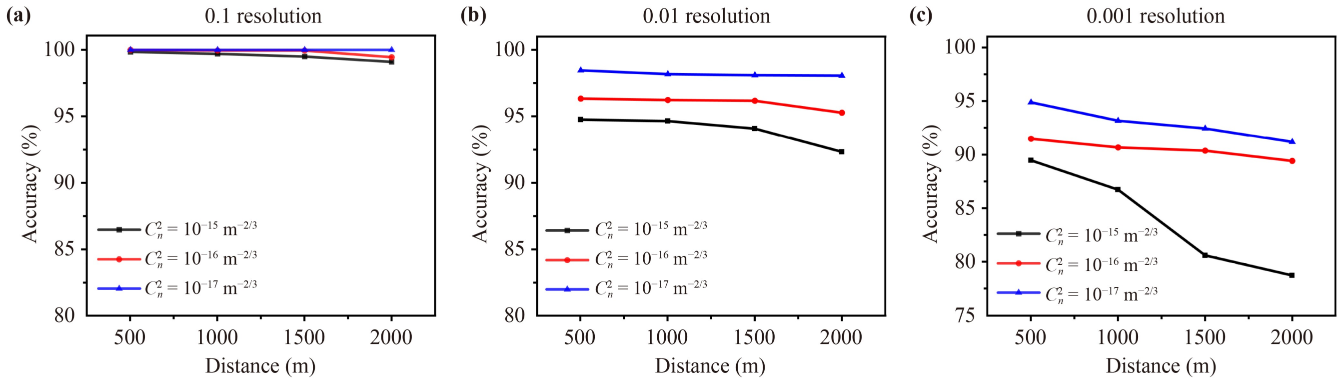

Fig. 7 Test accuracy of FOAM modes for different resolution under different AT and distances. **(a)** 0.1 resolution. **(b)** 0.01 resolution. **(c)** 0.001 resolution.

Table 1 Comparison of the improved EfficientNet V2 and ResNet 50 for the recognition of FOAM modes at 0.01 resolution under strong AT ($C_n^2 = 10^{-15}$ m$^{-2/3}$) and long transmission distance ($z = 1500$ m).

Model	Params	Dropout	Batch size	Lr	Optimizer	Time	Accuracy
ResNet 50	25.5 M	0.2	32	0.001	Adam	78 h	73.68%
Ours	24.3 M	0.2	32	0.005	Adam	54 h	93.98%

at 0.01 resolution still remains at a high level, further confirming the great effectiveness of our model. Figure 7(c) shows the recognition accuracy of FOAM modes at 0.001 resolution. With the increase of AT and transmission distance, the recognition accuracy decreases significantly. Under the weak AT ($C_n^2 = 10^{-17}$ m$^{-2/3}$), the recognition accuracy decreases to 94.88%, 93.17%, 92.45% and 91.18% with the increase of transmission distance. Under the medium AT ($C_n^2 = 10^{-16}$ m$^{-2/3}$), the recognition accuracy decreases to 91.48%, 90.67%, 90.37% and 89.42%. Under the strong AT ($C_n^2 = 10^{-15}$ m$^{-2/3}$), the recognition accuracy decreases to 89.47%, 86.73%, 80.63% and 78.77%. The above results show that the accuracy is relate to AT and remain high value even under strong AT.

In addition, compared with the ResNet 50 [32], our model shows significant improvement, especially under strong AT ($C_n^2 = 10^{-15}$ m$^{-2/3}$) and long transmission distance ($z = 1500$ m), the recognition accuracy is improved by 20.3% for the FOAM modes at 0.01 resolution. Furthermore, we also successfully realize the recognition of 0.001 FOAM modes. The specific comparative information for this improved EfficientNet V2 and ResNet 50 is shown in Table 1. It can be seen that our network is superior to ResNet 50 in terms of network complexity and training time, which greatly reduces the training time and computational resources. Therefore, our model has an advantage over the ResNet 50 in handling the task of FOAM recognition.

4 Conclusion

In conclusion, we propose an improved EfficientNet V2 based CNN model for the recognition of FOAM modes experimentally. By modifying the layers of the SE module and optimizing other parameters, the model has a better ability to extract image features. By learning the mapping relationship between the topological charge l and the intensity distribution of the FOAM modes after the AD, the different FOAM modes at 0.1, 0.01 and 0.001 resolution under strong AT and long transmission distance can be precisely recognized based on the model. Specifically, for the FOAM modes at 0.1, 0.01 and 0.001 resolution, the recognition accuracy is 99.12%, 92.24% and 78.77%, respectively, even in the presence of $C_n^2 = 10^{-15}$ m$^{-2/3}$ and $z = 2000$ m. These findings represent significant advancements in enhancing the channel capacity of FSO communication.

Declarations The authors declare that they have no competing interests and there are no conflicts.

Acknowledgements This work was supported by the National Natural Science Foundation of China (Grant Nos. 62271332, 12374273, and 62275162), the Guangdong Basic and Applied Basic Research Foundation (No. 2023A1515030152), the Shenzhen Government's Plan of Science and Technology (Nos. JCYJ20180305124927623 and JCYJ20190808150205481), and the Training Program for Excellent Young innovators of Changsha (No. kq2107013).

References

1. L. Allen, M. W. Beijersbergen, R. J. C. Spreeuw, and J. P. Woerdman, Orbital angular momentum of light and the transformation of Laguerre–Gaussian laser modes, *Phys. Rev. A* 45(11), 8185 (1992)
2. G. C. G. Berkhout, M. P. J. Lavery, J. Courtial, M. W. Beijersbergen, and M. J. Padgett, Efficient sorting of orbital angular momentum states of light, *Phys. Rev. Lett.* 105(15), 153601 (2010)
3. K. Liu, Y. Q. Cheng, X. Li, and Y. Gao, Microwave-sensing technology using orbital angular momentum: Overview of its advantages, *IEEE Veh. Technol. Mag.* 14(2), 112 (2019)
4. L. Yan, P. Kristensen, and S. Ramachandran, Vortex fibers for STED microscopy, *APL Photonics* 4(2), 022903 (2019)
5. X. W. Zhuang, Unraveling DNA condensation with optical tweezers, *Science* 305(5681), 188 (2004)
6. Z. Y. Zhou, D. S. Ding, Y. K. Jiang, Y. Li, S. Shi, X. S. Wang, and B. S. Shi, Orbital angular momentum light frequency conversion and interference with quasi-phase matching crystals, *Opt. Express* 22(17), 20298 (2014)
7. S. J. Li, Z. Y. Li, G. S. Huang, X. B. Liu, R. Q. Li, and X. Y. Cao, Digital coding transmissive metasurface for multi-OAM-beam, *Front. Phys.* 17(6), 62501 (2022)
8. L. Zou, L. Wang, and S. M. Zhao, Turbulence mitigation scheme based on spatial diversity in orbital-angular-momentum multiplexed system, *Opt. Commun.* 400, 123 (2017)
9. E. M. Amhoud, M. Chafii, A. Nimr, and G. Fettweis, OFDM with index modulation in orbital angular momentum multiplexed free space optical links, in: IEEE 93rd Vehicular Technology Conference (VTC-Spring), Electr Network, 2021
10. A. E. Willner, K. Pang, H. Song, K. H. Zou, and H. B. Zhou, Orbital angular momentum of light for communications, *Appl. Phys. Rev.* 8(4), 041312 (2021)
11. X. H. Zhang, T. Xia, S. B. Cheng, and S. H. Tao, Free-space information transfer using the elliptic vortex

beam with fractional topological charge, *Opt. Commun.* 431, 238 (2019)

12. V. V. Kotlyar, A. A. Kovalev, A. G. Nalimov, and A. P. Porfirev, Evolution of an optical vortex with an initial fractional topological charge, *Phys. Rev. A* 102(2), 023516 (2020)
13. S. S. Li, B. F. Shen, W. P. Wang, Z. G. Bu, H. Zhang, H. Zhang, and S. H. Zhai, Diffraction of relativistic vortex harmonics with fractional average orbital angular momentum, *Chin. Opt. Lett.* 17(5), 050501 (2019)
14. M. I. Dedo, Z. Wang, K. Guo, Y. Sun, F. Shen, H. Zhou, J. Gao, R. Sun, Z. Ding, and Z. Guo, Retrieving performances of vortex beams with GS algorithm after transmitting in different types of turbulences, *Appl. Sci. (Basel)* 9(11), 2269 (2019)
15. X. Yan, P. F. Zhang, J. H. Zhang, X. X. Feng, C. H. Qiao, and C. Y. Fan, Effect of atmospheric turbulence on entangled orbital angular momentum three-qubit state, *Chin. Phys. B* 26(6), 064202 (2017)
16. Y. J. Yang, Q. Zhao, L. L. Liu, Y. D. Liu, C. Rosales-Guzman, and C. W. Qiu, Manipulation of orbital-angular-momentum spectrum using pinhole plates, *Phys. Rev. Appl.* 12(6), 064007 (2019)
17. Z. C. Zhang, J. C. Pei, Y. P. Wang, and X. G. Wang, Measuring orbital angular momentum of vortex beams in optomechanics, *Front. Phys.* 16(3), 32503 (2021)
18. A. Forbes, A. Dudley, and M. McLaren, Creation and detection of optical modes with spatial light modulators, *Adv. Opt. Photonics* 8(2), 200 (2016)
19. J. Yu and Z. F. Wang, 3D facial motion tracking by combining online appearance model and cylinder head model in particle filtering, *Sci. China Inf. Sci.* 57(7), 029101 (2014)
20. N. Uribe-Patarroyo, A. Fraine, D. S. Simon, O. Minaeva, and A. V. Sergienko, Object identification using correlated orbital angular momentum states, *Phys. Rev. Lett.* 110(4), 043601 (2013)
21. J. Zhu, P. Zhang, D. Z. Fu, D. X. Chen, R. F. Liu, Y. N. Zhou, H. Gao, and F. L. Li, Probing the fractional topological charge of a vortex light beam by using dynamic angular double slits, *Photon. Res.* 4(5), 187 (2016)
22. D. Deng, M. C. Lin, Y. Li, and H. Zhao, Precision measurement of fractional orbital angular momentum, *Phys. Rev. Appl.* 12(1), 014048 (2019)
23. S. Zheng and J. Wang, Measuring orbital angular momentum (OAM) states of vortex beams with annular gratings, *Sci. Rep.* 7(1), 40781 (2017)
24. K. Bayoudh, R. Knani, F. Hamdaoui, and A. Mtibaa, A survey on deep multimodal learning for computer vision: Advances, trends, applications, and datasets, *Vis. Comput.* 38(8), 2939 (2022)
25. N. O'Mahony, S. Campbell, A. Carvalho, S. Harapanahalli, G. V. Hernandez, L. Krpalkova, D. Riordan, and J. Walsh, Deep learning vs. traditional computer vision, in: Computer Vision Conference (CVC), Springer International Publishing Ag, Las Vegas, NV, 2019, pp 128–144
26. J. Long, E. Shelhamer, and T. Darrell, Fully convolutional networks for semantic segmentation, in: IEEE Conference on Computer, Vision and Pattern Recognition (CVPR), IEEE, Boston, MA, 2015, pp 3431–3440
27. N. Le, V. S. Rathour, K. Yamazaki, K. Luu, and M. Savvides, Deep reinforcement learning in computer vision: a comprehensive survey, *Artif. Intell. Rev.* 55(4), 2733 (2022)
28. R. Yamashita, M. Nishio, R. K. G. Do, and K. Togashi, Convolutional neural networks: An overview and application in radiology, *Insights Imaging* 9(4), 611 (2018)
29. P. Michalski, B. Ruszczak, and M. Tomaszewski, Convolutional neural networks implementations for computer vision, in: 3rd International Scientific Conference on Brain-Computer Interfaces (BCI), Springer International Publishing Ag, Opole Univ Technol, Opole, POLAND, 2018, pp 98–110
30. Z. W. Liu, S. Yan, H. G. Liu, and X. F. Chen, Superhigh-resolution recognition of optical vortex modes assisted by a deep-learning method, *Phys. Rev. Lett.* 123(18), 183902 (2019)
31. M. Cao, Y. L. Yin, J. W. Zhou, J. H. Tang, L. P. Cao, Y. Xia, and J. P. Yin, Machine learning based accurate recognition of fractional optical vortex modes in atmospheric environment, *Appl. Phys. Lett.* 119(14), 141103 (2021)
32. J. Zhou, Y. Yin, J. Tang, C. Ling, M. Cao, L. Cao, G. Liu, J. Yin, and Y. Xia, Recognition of high-resolution optical vortex modes with deep residual learning, *Phys. Rev. A* 106(1), 013519 (2022)
33. W. W. Song, S. T. Li, L. Y. Fang, and T. Lu, Hyperspectral image classification with deep feature fusion network, *IEEE Trans. Geosci. Remote Sens.* 56(6), 3173 (2018)
34. M. X. Tan and Q. V. Le, EfficientNetV2: Smaller models and faster training, in: International Conference on Machine Learning (ICML), Electr Network, 2021, pp 7102–7110
35. M. L. Huang and Y. C. Liao, A lightweight CNN-based network on COVID-19 detection using X-ray and CT images, *Comput. Biol. Med.* 146, 105604 (2022)
36. R. Karthik, T. S. Vaichole, S. K. Kulkarni, O. Yadav, and F. Khan, Eff2Net: An efficient channel attention-based convolutional neural network for skin disease classification, *Biomed. Signal Process. Control* 73, 103406 (2022)
37. H. Zhang, J. Zeng, X. Y. Lu, Z. Y. Wang, C. L. Zhao, and Y. J. Cai, Review on fractional vortex beam, *Nanophotonics* 11(2), 241 (2022)
38. A. Belafhal and L. Dalil-Essakali, Collins formula and propagation of Bessel-modulated Gaussian light beams through an ABCD optical system, *Opt. Commun.* 177(1–6), 181 (2000)
39. Y. J. Yang, Y. Dong, C. L. Zhao, and Y. J. Cai, Generation and propagation of an anomalous vortex beam, *Opt. Lett.* 38(24), 5418 (2013)
40. P. H. F. Mesquita, A. J. Jesus-Silva, E. J. S. Fonseca, and J. M. Hickmann, Engineering a square truncated lattice with light's orbital angular momentum, *Opt. Express* 19(21), 20616 (2011)
41. B. Rodenburg, M. P. J. Lavery, M. Malik, M. N. O' Sullivan, M. Mirhosseini, D. J. Robertson, M. Padgett, and R. W. Boyd, Influence of atmospheric turbulence on states of light carrying orbital angular momentum, *Opt. Lett.* 37(17), 3735 (2012)

42. S. Y. Fu and C. Q. Gao, Influences of atmospheric turbulence effects on the orbital angular momentum spectra of vortex beams, *Photon. Res.* 4(5), B1 (2016)
43. L. C. Andrews, An analytical model for the refractive index power spectrum and its application to optical scintillations in the atmosphere, *J. Mod. Opt.* 39(9), 1849 (1992)
44. W. Cheng, J. W. Haus, and Q. W. Zhan, Propagation of vector vortex beams through a turbulent atmosphere, *Opt. Express* 17(20), 17829 (2009)
45. S. M. Zhao, J. Leach, L. Y. Gong, J. Ding, and B. Y. Zheng, Aberration corrections for free-space optical communications in atmosphere turbulence using orbital angular momentum states, *Opt. Express* 20(1), 452 (2012)
46. Y. Kim, I. Ohn, and D. Kim, Fast convergence rates of deep neural networks for classification, *Neural Netw.* 138, 179 (2021)